

# A pattern in the imaging data: mere artefact of spatio-temporal resolution

Swayamshree Patra<sup>1</sup>, Swagata Dey<sup>2,3</sup>, Krishanu Ray<sup>2</sup>, Debashish Chowdhury<sup>1\*</sup>

<sup>1</sup>*Department of Physics, Indian Institute of Technology Kanpur, 208016, India ;*

<sup>2</sup>*Department of Biological Sciences, Tata Institute of Fundamental Research, Mumbai, 400005, India ;*

<sup>3</sup>*Current Address: National Brain Research Centre, Manesar, 122052, India*

' *Seeing is believing* ' [1]- is the fundamental philosophy of optical imaging based on light microscopy [2]. Since the pioneering works of Antonie van Leeuwenhoek and Robert Hooke in the 17th century, optical microscopy has served as one of the most important tools in biological sciences [3]. But interpreting visual observations with preconceived notions can potentially mislead one to erroneous conclusions. Here we report one such case where, at first sight, the interesting pattern extracted from the images of axonal transport may appear to reveal some hitherto unknown features of cargo transport driven by cytoskeletal motors [4]. It may even be tempting to theorize about the possible molecular mechanisms that could give rise the observed pattern. But, as we conclusively demonstrate here, these patterns are mere artifacts of the spatial and temporal resolutions of imaging microscopes. These observed patterns, and their interpretations, are rather universal in the sense that in all those experiments where an observer (or machine), having limited spatial and temporal resolution, tracks the movement of classical objects moving on a one-dimensional track, such enticing patterns will invariably emerge. Our analysis here exposes pitfalls lurking in the way one interprets such patterns; unless critically analyzed, believing in whatever one is seeing, one could draw an illusory conclusion.

The primary goal of our research is to infer the traffic rules for the motor-driven transport of intracellular cargoes like vesicles and organelles [5, 6]. Long range translocation of assorted cargoes to different locations, with customized mechanisms, along the conduit-shaped axon makes axonal transport as one of the most challenging problems of transport logistics [7–11]. Fluorescently tagged cargoes have facilitated live observation [12–14] of transport phenomena which are, for quantification purposes, further represented as kymographs that graphically depict the spatial positions of the cargoes over time. Whole trajectory of each cargo (vesicle and organelle) imprinted on the space-time diagrams (kymographs) give wealth of information about the mechanisms of their motility. Similarly, the whole trajectories of multiple cargoes simultaneously imprinted on the space-time diagrams provide a global picture of the intracellular traffic. For example, criss crossing trajectories of anterograde and retrograde vesicles [15, 16] and neurofilaments [17] are associated with their bidirectional transport in axon, merging and splitting trajectories reveal the fusion and fission dynamics of trains in flagellar transport [18, 19] and vertical lines mark regions of traffic jams [20]. In this paper we analyze data collected by optical imaging of cytoskeletal motor driven transport of Rab4 associated vesicles in *Drosophila* neurons [16].

An individual straight segment is a part of track along which the velocity remains constant. If the cargo under observation displays bidirectional motion (Fig. 1A), it is recommended to segregate the anterograde and retrograde runs as individual segmental runs (Fig. 1B). Two primary quantitative characteristics that are routinely extracted from kymographs are the run length, which is the distance covered, and the run time, which is the time taken by the cargo to finish each segmental run. In terms of the pixel size, which determines the spatial resolution  $\Delta\ell$ , the run length is given by

$$\text{Run length} = \text{pixel size} * (d_e - d_b) = \Delta\ell * (d_e - d_b) \quad (1)$$

where  $d_b$  is the X-axis coordinate in the frame in which the segmental run begins and  $d_e$  is the X-axis coordinate in the frame in which the segmental run ends (See Fig. 1C and Fig. 1D). Similarly, in terms of the frame rate, which is inversely related to the temporal resolution  $\Delta t$ , the run time is given by

$$\text{Run time} = \frac{1}{\text{frame rate}} * \text{number of frames} = \Delta t * \text{number of frames} \quad (2)$$

where the number of frames is the difference between the frame number in which the segmental run begins and the frame number in which the segmental run ends (Fig. 1D). Combining the definitions of run length and run time, the

---

\* Corresponding author (E-mail: debch@iitk.ac.in)

segmental velocity can be expressed as

$$\text{Velocity} = \text{pixel size} * \text{frame rate} * \frac{(d_e - d_b)}{\text{number of frames}} = \frac{\Delta \ell}{\Delta t} * \frac{(d_e - d_b)}{\text{number of frames}} \quad (3)$$

The run lengths of the segments on the kymograph and the corresponding velocities were taken as the readouts of the individual runs. From these distributions of individual run-lengths and velocities, the average run length and average velocity, respectively, could be calculated. The frequency distribution of Rab4 associated vesicles in lch5 neurons of *Drosophila* showed their velocities as a single mode Gaussian whereas that of the run lengths was found to be multimodal, i.e., a distribution with multiple peaks (Fig. 1E) [16]. With such multimodal distributions, it is difficult to predict the correlation of these two pivotal quantities, namely the run length and the velocity, that characterise intracellular transport. So we tried to visualize their interdependence in a scatter plot where run lengths are plotted along Y-axis as a function of their corresponding velocities along the X-axis. Although we expected that points to form some local clusters, but the scatter plot emerged with fascinating patterns having many inexplicable features (Fig. 1F).

The first attribute is the segregation of points in the scatter plot into a peculiar tent like cluster (Fig. 1F). Imagine a tent with multiple fly-sheets arranged coaxially on a horizontal rod and loosely pitched on the ground. The whole arrangement has to be supported by a vertical pole (Fig. 2A). A projection of the frontal view of the tent is what the cluster with multiple number of stacked curves, forming cusps on the centrally located vertical isovels at velocity  $v_c$ , look like. An isovel is a vertical line on this plot at a given velocity  $v_c$ ; thus, velocity  $v_c$  remains constant along an isovel and hence the name. Next is the appearance of tent-like patterns at regular intervals like a single row of equispaced tents of increasing height fixed side-by-side in a field (Fig. 2B). This associated spatial periodicity along the velocity axis (X-axis) is the second surprising attribute of the correlation plot. The third is the exactly identical features of both anterograde and retrograde scatter plots - like the same curvature of curves and their same locations giving rise to exactly equal periodicity along the horizontal axis. On superposing both the anterograde and retrograde plots, their significant overlap further emboldens the claim that anterograde and retrograde plots are practically identical (Fig. 2C).

Now we show how one might attempt to account for the observed data in terms of a plausible mechanisms of intracellular transport of cargoes by cooperating and competing cytoskeletal motors [8]. Let us begin with the individual tent-like patterns (Fig. 2A). The tendency of a pair of curves to form cusp around an isovel located centrally at a particular velocity  $v_c$  presents the scenario where a motor-cargo complex, with this tailor-made velocity  $v_c$ , steers through the dynamic and static roadblocks along the axon processively. However, because of intrinsic fluctuations or extrinsic hindrances in the crowded environment, slight deviations from this velocity could adversely affect the motility of the cargo thereby resulting in shorter runlengths. This argument could explain the decreasing curves around the isovels.

At first sight, it may appear that the scenario envisaged above would be consistent also with the spatial periodicity of the tent-like clusters, which is the second feature of the patterns on the scatter plot (Fig. 2B). The presence of multiple clusters at different velocities indicates the possibility that the cargo-motor complexes move with multimodal velocity distribution [21]. The multiple peaks may be a consequence of either the innate property of the associated individual motors or the emergent property of the motor-cargo complex where a group of motors is collectively carrying the cargo. In principle, motors moving in the same direction could team up to generate higher force and velocity [22]. For example, the vesicles associated with a single motor register runs which will belong to the first cluster (leftmost tent-line pattern), the second cluster represent those vesicles which are carried by two motors and so on. Motors belonging to the kinesin family can cooperate among themselves as do the dyneins and this explains the periodic patterns in both anterograde and retrograde plot (Fig. 1F). The above arguments may be appealing and one may be tempted to conclude that, with the heuristic arguments presented here, one could explain the appearance of multiple tent-like shapes at periodic locations in the observed pattern.

But the the third feature of the pattern, namely the fact that both the scatter plots representing anterograde and retrograde runs are quite similar (Fig. 2C) raises serious objections against the validity of the plausible interpretation of the observed patterns described above. Kinesins and dyneins do not have the exactly same *in-vivo* velocities [6]. Moreover, the theory regarding the cusps is incapable of explaining the presence of a bunch of curves stacked over one another in the tent-like cluster forming cusps on a single central isovel (Fig. 2A). Thus, one has to look for an alternative interpretation of the observed patterns in the imaging data.

In our MC simulations, we monitored the stochastic movement of a single vesicle along a one-dimensional chain with equispaced sites [23]. For details please see the Methods and SI figure 1. In order that this chain mimics a microtubule the gap between the successive sites was chosen to be 8 nm. The movement of the vesicle was recorded by a virtual camera having a fixed pixel size (spatial resolution)  $\Delta \ell$  and the acquisition time for an individual frame (temporal resolution) is  $\Delta t$ . Multiple trajectories were recorded on the kymographs by repeating the simulations and segmental runs were extracted from these trajectories as discussed in Fig. 1 (See SI Fig. 2). The run length and

run time of individual run, obtained from the digital kymographs, were integral multiples of  $\Delta\ell$  and  $\Delta t$ , respectively. Again the tent-like patterns were observed in the correlation plot of velocity and run length. Interestingly, the clusters of points in the pattern shifted, widened or narrowed on changing the spatial and temporal resolutions, indicating that the limited resolving capability of the acquisition system is responsible for emergence of such a pattern (See SI Fig. 3). So, in the rest of the communication, with a simple thought experiment we demonstrate how the interplay of space and time resolution leads to the emergence of the pattern in the imaging data.

The thought experiment is a tracking experiment with a bunch of color-coded balls moving smoothly on a one-dimensional multilane track. The balls are color coded according to their velocities. The experiment starts with the balls being lined up at the starting point of the multi-lane track of length  $L$ . They are arranged according to their velocities - with the slowest one at one end (red ball) and the fastest one at the other (green ball) (see Fig. 1A). Although all the balls start moving simultaneously towards the finish point on their respective tracks, but ultimately their velocities determine the time they take to finish the journey. The whole process is captured in a series of snapshots of certain pixels taken at regular interval by an imaginary camera. In our thought experiment, the pixel size is  $\Delta\ell = 0.1\mu\text{m}$  and the acquisition time per snapshot/frame is  $\Delta t = 0.2\text{ s}$ . The track length  $L$  is expressed as an integral multiple of  $\Delta\ell$  ( $L = n_\ell\Delta\ell$ ;  $n_\ell$  is a positive integer). The velocity of the balls are pre-programmed in such a way that if the fastest ball(green) covers the entire length in  $n_t$  frames, i.e, after  $n_t\Delta t$  seconds, then to finish the move the second fastest ball will take  $(n_t + 1)\Delta t$  seconds, the third fastest will take  $(n_t + 2)\Delta t$  seconds and so on ( $n_t$  is a positive integer).

The first five snapshot of a particular case in our thought experiment are shown in figure 3A. The corresponding segmental runs of the balls are analysed on kymographs which is made by stacking the snapshots (see Fig. 3B). We repeat the tracking experiment with tracks of different length  $L$  and we have shown the kymographs for three cases (see Fig. 3B): Set-1 (track of length  $1.0\mu\text{m}$ ), Set-2 (track of length  $1.5\mu\text{m}$ ) and Set-3 (track of length  $2.0\mu\text{m}$ ). Because of the simple choice of the velocities of the balls, as explained above, the segmental runs of the balls end on consecutive pixels (see Fig. 3B) in the last column of the kymographs. We have imposed a condition that the speed of the fastest ball cannot exceed  $5\mu\text{m/s}$ . As a consequence, the time taken by the fastest ball moving at a speed  $5\mu\text{m/s}$  to cover  $1.0\mu\text{m}$  or  $2.0\mu\text{m}$  is  $1\Delta t$  s or  $2\Delta t$  s respectively (See Set-1 and Set-3 in Fig 3B). But the shortest time in which the fastest ball can cover a track of some inbetween resolvable length say  $1.5\mu\text{m}$ , will be  $2\Delta t$  s (with a speed  $1.5\mu\text{m}/2\Delta t = 3.75\mu\text{m/s}$ ) because if it covers this length in  $1\Delta t$ s, then the speed it should pose will be more than the speed limit of  $5.0\mu\text{m/s}$  which we don't allow (See Set-2 in figure 3B). This indicates that due to the finite spatial and temporal resolutions, the run lengths of all segmental runs must have certain discrete values and there has to be a set of discrete velocities with which each runlength can be covered.

From each Set (kymographs in Fig. 3B), we get an ensemble of runs having same runlength but different velocities. Hence, plotting the velocities and the corresponding run lengths obtained from a particular kymograph on the correlation plot we get an isorun, which is a horizontal line along which the run length remains constant (see Fig. 3C). Now repeating the experiment with tracks of different length and analyzing the runs on different kymographs, we get isoruns having different runlength. By stacking the isoruns collected from different sets of experiments, a pattern with a periodic sequence of tent-like structures emerges in the correlation plot indicating this pattern to be a mere artifact of spatio-temporal resolution.

From the scatter plot in figure 3C, we conclude that the isovels, which are the centre of the tent-like clusters, occur at velocities which are integral multiple of the velocity given by  $\Delta\ell/\Delta t$ . In our thought experiment with  $\Delta\ell = 0.1\mu\text{m}$  and  $\Delta t = 0.2\text{ s}$ , we observed isovels at velocities which are integral multiple of  $0.5\mu\text{m/s}$  ( $=0.1\mu\text{m}/0.2\text{ s}$ ) (Fig. 3C). And as the spatial resolution of the confocal microscope is  $\Delta\ell = 0.115\mu\text{m}$  and temporal resolution is  $\Delta t = 0.2\text{ s}$ , we observed isovels, at velocities that are integral multiple of  $0.575\mu\text{m/s}$  ( $=0.115\mu\text{m}/0.2\text{ s}$ ) (Fig 2B). The curves in the  $m^{\text{th}}$  cluster, which surround the  $m^{\text{th}}$  isovel, can also be expressed in terms  $\Delta\ell$  and  $\Delta t$ . The equation of the  $n^{\text{th}}$  curve around the  $m^{\text{th}}$  isovel (Fig. 3C) is given by

$$v = \frac{r \left\{ \frac{m\Delta\ell}{\Delta t} \right\}}{r + n\Delta\ell} \quad (4)$$

where  $v$  is the velocity,  $r$  is the run length,  $m = 1, 2, 3, \dots$  and  $n = \dots, -1, 0, 1, \dots$

As both the anterograde and retrograde runs are captured by the same microscope, with the same spatio-temporal resolution, identical patterns emerge in the velocity-run length correlation plot. Thus, our simple explanation for the physical origin of the non-trivial pattern demystifies the perplexing feature that both the anterograde and retrograde plots are practically identical, irrespective of the motor-cargo complex that one is observing.

In order to explore how the pattern varies with the variation of the spatial and temporal resolution of the microscope, we coarse grained the available kymographs. The underlying principle of this coarse graining could be understood from figure 4A. When a line segment is measured on a ruler of finer least count, the length is reported as the number of

unit cells ( $n_f$ ) in the bounding rectangle multiplied by the length of one unit cell (least count- $\Delta x_f$ ). Let the length of the segment when measured on a finer scale be  $L_f (= \Delta x_f \times n_f)$ . But when the same is measured on the coarser scale with least count  $\Delta x_c$  greater than  $\Delta x_f$ , we get the length as  $L_c (= \Delta x_c \times n_c)$  ( $n_c$  is the number of unit cells in the bounding rectangle on the ruler with coarser scale). And we say that length of the segment has been coarse-grained. The length of the segment measured on rulers of different scales has been summarised on the complementary table in figure 4A. Based on this concept, we measure the projections of the segmental runs on  $x$ -axis (run-length) and  $y$ -axis (run-time) in the coarse grained kymographs as illustrated in figure 4B.

We choose three kymographs with different pixel size and acquisition time indicated below the respective kymographs. Qualitatively, the resolution associated with each pixel could be compared by the colored cell at the corner of each kymograph (Kymograph-1(red); Kymograph-2(green); Kymograph-3(blue) in figure 4B). We analysed twelve resolvable segmental runs having same velocity but different runlength on kymograph-1 with finer scale. But out of the 12, only 6 and 3 runs marked by the solid lines are perfectly resolvable on kymograph-2 and kymograph-3 respectively. The other runs marked by the dotted lines are not perfectly resolvable, but the cells in which the run begins and the one in which the run ends will determine the magnitude of run length and run time. In figure. 4C we have plotted the isovels measured from these three different kymographs. As we coarse grain the data, number of points in the isovel decreases. In figure 4D, we fitted the original anterograde data obtained from the in-vivo experiment in Plot-1. If the same system is imaged by microscopes having spatial and temporal resolution indicated in Plot-2 and Plot-3, then the points will lie on the curves given by equation (4).

Kymographs are raster images (grids of pixels), where the dimensions of the individual pixels represent length and time and their magnitudes are measures of the spatial and temporal resolution, respectively. Measuring the projections of runs for the run time and runlength on this raster image leads to discrete values of runlength and velocity. When displacement is plotted as a function of velocity for understanding their codependency, the segregation of points into tent shaped clusters, the pattern at first sight may appear to indicate deep underlying physical processes. But as we demonstrated here, the patterns are mere artifact of finite spatio-temporal resolution. Rather than getting misled at the first glance by the biases we harbour, complementing the observation with some simple but concrete theory could save one from erroneous interpretation of the observation [24–26]. So we conclude with the message - " *Seeing is believing, but believing blindly could be deceiving* ".

## I. AUTHOR CONTRIBUTION

S.P., K.R. and D.C. designed research. S.D. and K.R. provided the experimental data. S.P. and D.C. developed the theoretical framework. S.P. did the computer simulations and analyzed the simulation data. S.P. S.D. and D.C. wrote the paper.

## II. ACKNOWLEDGEMENT

SP thanks Manoj Harbola for stimulating discussions, and Annwesha Dutta, Ashish Kumar, Bhavya Mishra for some critical comments on the figures. SP, KR and DC thank ICTS for the hospitality during the ICTS Discussion Meeting "Collective Dynamics of-, on- and around Filaments in Living Cells: Motors, MAPs, TIPs and Tracks 2017", where a part of this work was done. This work has been supported by a J.C. Bose National Fellowship (DC), the Prof. S. Sampath Chair Professorship (DC) and an intramural grant of TIFR, DAE, Govt. of India (KR).

## III. REFERENCES

- 
- [1] North, A. Seeing is believing? A beginners' guide to practical pitfalls in image acquisition. *The Journal of Cell Biology* **172**, 9-18 (2006).
  - [2] Ntziachristos, V. Going deeper than microscopy: the optical imaging frontier in biology. *Nature Methods* **7**, 603-614 (2010).
  - [3] Thorn, K. A quick guide to light microscopy in cell biology. *Molecular Biology of the Cell* **27**, 219-222 (2016).
  - [4] Ross, J. L. The Dark Matter of Biology. *Biophysical Journal* **111**, 909916 (2016).
  - [5] Chowdhury, D. Stochastic mechano-chemical kinetics of molecular motors: a multidisciplinary enterprise from a physicist's perspective. *Phys. Rep.* 529, 1-197 (2013).
  - [6] Howard, J. Mechanics of Motor Proteins and the Cytoskeleton *Sinauer Associates* 2001

- [7] Goldstein, L.S.B. Do disorders of movement cause movement disorders and dementia. *Neuron* **40**, 415-425 (2003)
- [8] Encalada, S. & Goldstein, L. Biophysical Challenges to Axonal Transport: Motor-Cargo Deficiencies and Neurodegeneration. *Annual Review of Biophysics* **43**, 141-169 (2014).
- [9] Hirokawa, N., Niwa, S., Tanaka, Y. Molecular Motors in Neurons: Transport Mechanisms and Roles in Brain Function, Development, and Disease. *Neuron* **68** 610-638 (2010.)
- [10] Brown, A. Axonal transport of membranous and nonmembranous cargoes. *The Journal of Cell Biology* **160**, 817821 (2003).
- [11] Hancock, W.O., Bidirectional cargo transport: moving beyond tug of war. *Nature Reviews Molecular Cell Biology* **15**, 615628 (2014)
- [12] Liu, Z., Lavis, D.L., & Betzig, E., Imaging Live-Cell Dynamics and Structure at the Single-Molecule Level. *Molecular Cell* **58**, 644-659 (2015).
- [13] Bohner, G., Gustafsson, N., Cade, N.I., Maurer, S.P., Griffin, L.D., and Surrey, T., Important factors determining the nanoscale tracking precision of dynamic microtubule ends. *Journal of Microscopy* **261**, 6778 (2016).
- [14] Ruhnnow, F., Klo, L. & Diez, S. Challenges in Estimating the Motility Parameters of Single Processive Motor Proteins. *Biophysical Journal* **113**, 24332443 (2017).
- [15] Kulkarni, A., Khan, Y., & Ray, K. Heterotrimeric kinesin-2, together with kinesin-1, steers vesicular acetylcholinesterase movements toward the synapse. *FASEB J.* **31**, 965974 (2017).
- [16] Dey, S., Banker, G. & Ray, K. Anterograde Transport of Rab4-Associated Vesicles Regulates Synapse Organization in *Drosophila*. *Cell Reports* **18**, 2452-2463 (2017).
- [17] Fenn, J., Johnson, C., Peng, J., Jung, P. & Brown, A. Kymograph analysis with high temporal resolution reveals new features of neurofilament transport kinetics. *Cytoskeleton* **75**, 22-41 (2017).
- [18] Buisson, J. et al. Intraflagellar transport proteins cycle between the flagellum and its base. *Journal of Cell Science* **126**, 327-338 (2012).
- [19] Stepanek, L. & Pigino, G. Microtubule doublets are double-track railways for intraflagellar transport trains. *Science* **352**, 721-724 (2016).
- [20] Sood, P. et al. Cargo crowding at actin-rich regions along axons causes local traffic jams. *Traffic* **19**, 166-181 (2018).
- [21] Reis, G. et al. Molecular motor function in axonal transport in vivo probed by genetic and computational analysis in *Drosophila*. *Molecular Biology of the Cell* **23**, 1700-1714 (2012).
- [22] Klumpp, S. & Lipowsky, R. Cooperative cargo transport by several molecular motors. *Proceedings of the National Academy of Sciences* **102**, 17284-17289 (2005).
- [23] Schadschneider, A., Chowdhury, D., & Nishinari, K. Stochastic transport in complex systems: from molecules to vehicles. *Elsevier* (2010).
- [24] Waters, J.C. Accuracy and precision in quantitative fluorescence microscopy. *J. Cell Biol.* **185**, 1135-1148 (2009).
- [25] Frigault, M.M., Lacoste, J., Swift, J.L., Brown, C. M. Live-cell microscopy- tips and tools. *J. Cell Sci.* **122**, 753-767 (2009).
- [26] Howard, J. Quantitative cell biology: the essential role of theory. *Molecular Biology of the Cell* **25**, 34383440 (2014).

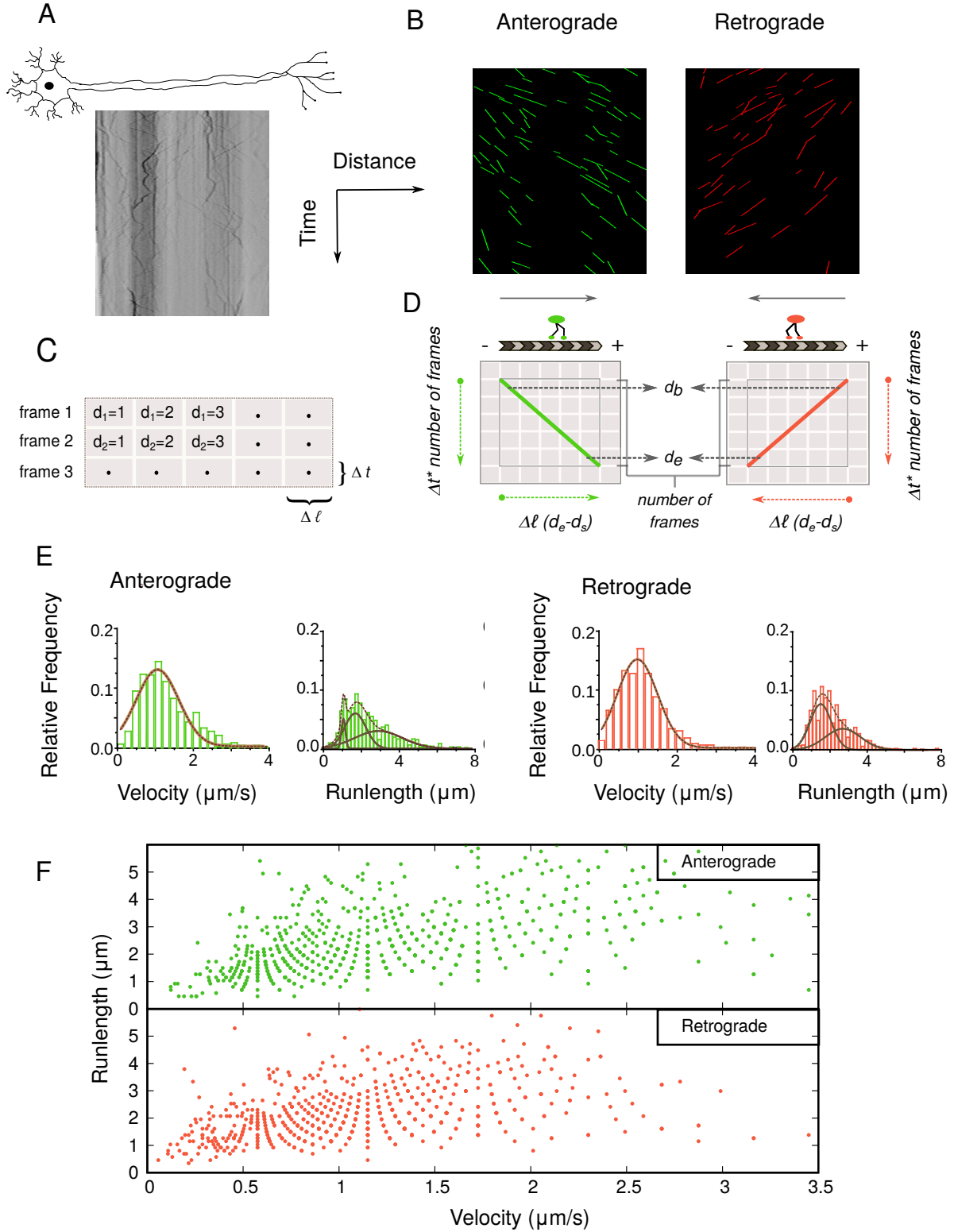


**FIG. 1: Extraction and quantification of segmental runs:** (A) Kymograph encoding the movement of Rab4 associated vesicles undergoing axonal transport in *Drosophila* neurons. (B) Segmental runs in anterograde (green) and retrograde (red) direction extracted from the original kymograph shown in A. (C) Kymograph is a stack of frames captured at regular interval of time. Each frame is a row of pixels and the  $m^{\text{th}}$  pixel in the  $n^{\text{th}}$  frame is denoted by  $d_n = m$  (where  $m$  and  $n$  are positive integers). Pixel size given by the length of the pixel determines the spatial resolution  $\Delta \ell$  and width of the frame represents the temporal resolution  $\Delta t$ . (D) A segmental anterograde and retrograde run on a zoomed kymograph (which is a grid of pixels).  $d_b$  is the X-axis coordinate in the frame in which the segmental run begins and  $d_e$  is the X-axis coordinate in the frame in which the segmental run ends. Projection of the segmental run on x-axis gives the run length and projection on y-axis gives the run time. (E) The velocity distribution in both anterograde and retrograde directions are fitted with a Gaussian distribution. The runlengths in both direction are fitted with multimodal curve fit where each mode is fitted with individual Gaussian distribution. (F) In the scatter plots, runlengths extracted from the segmental run in both anterograde and retrograde direction are plotted as a function of the corresponding velocities.



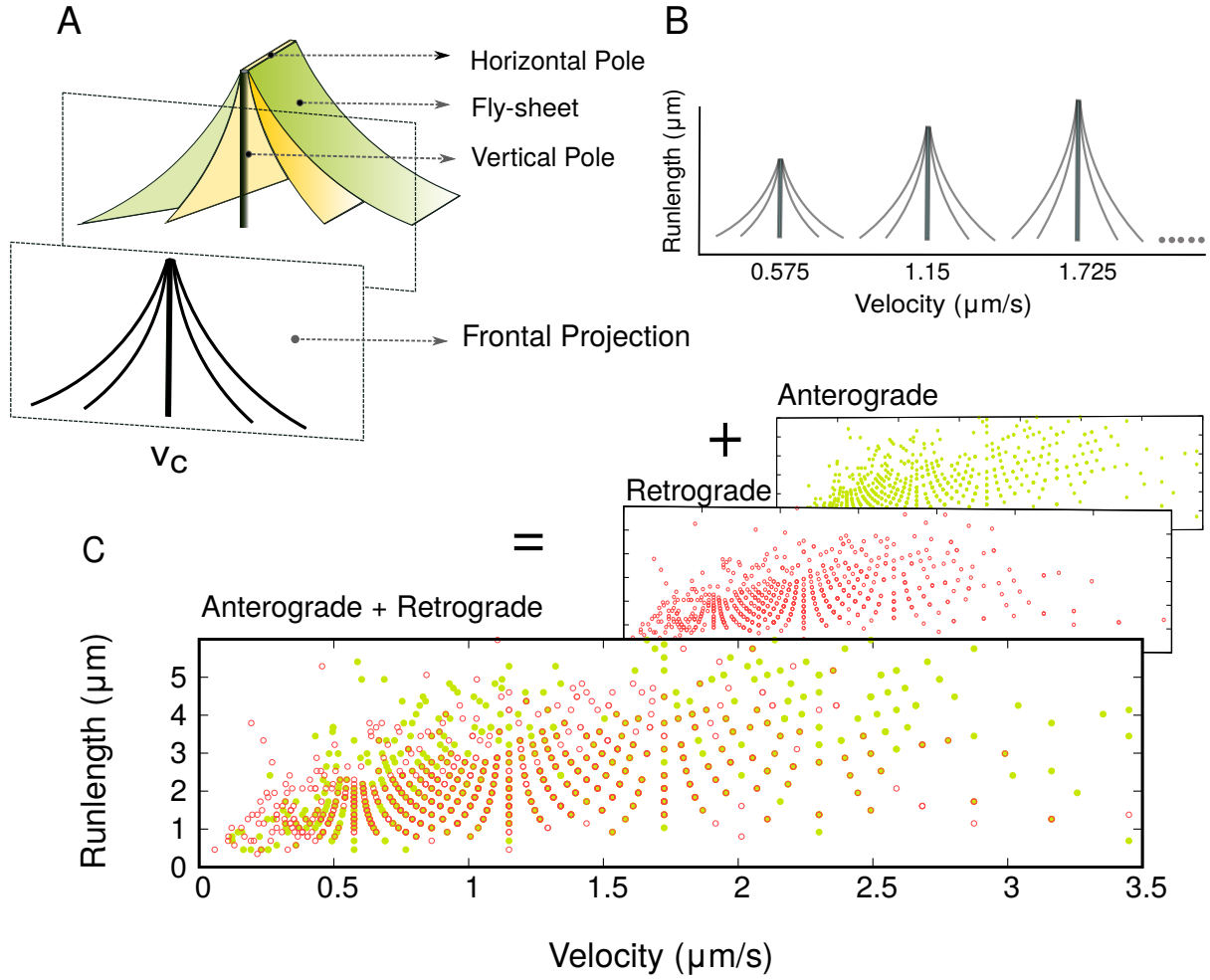
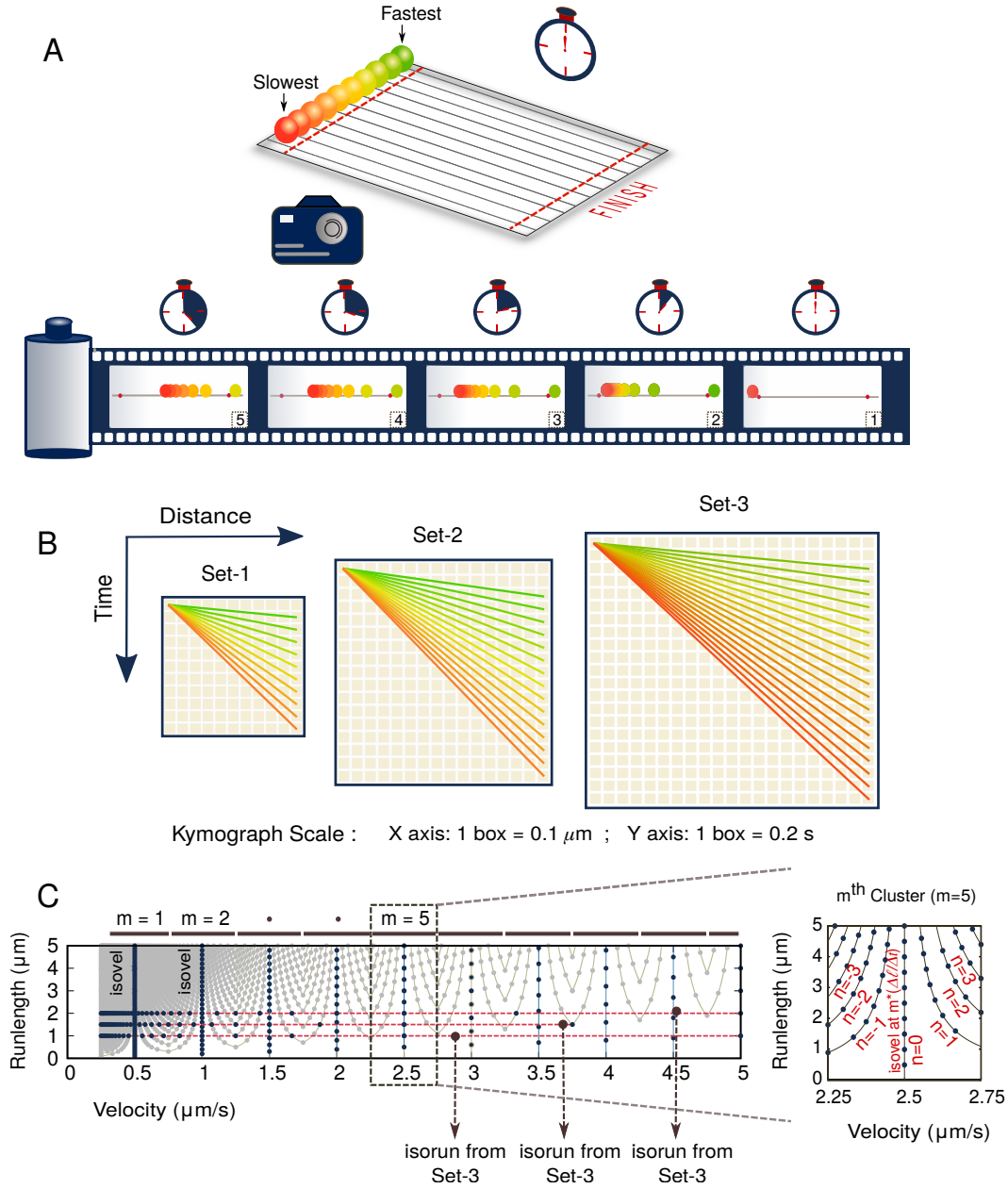


FIG. 2: **Features of correlation plot:** (A) A tent with multiple flysheets supported by a central vertical pole. A frontal projection of this tent resembles the pattern of the clusters that appear in the velocity-runlength correlation plots. In each cluster, there are multiple curves stacked on each other and they form cusp on the centrally located vertical isovel at velocity  $v_c$ . (B) Multiple clusters appearing at regular intervals look like a row of equispaced tents of increasing height. These clusters are centred around their corresponding isovels at velocities  $v_c$  which are integral multiples of  $0.575 \mu\text{m/s}$ . (C) Superposition of anterograde and retrograde correlation plots shows a significant overlap.

**A pattern in the imaging data: mere artefact of spatio-temporal resolution:**  
Methods Supplementary Information

**Drosophila stocks, culture and sample preparation**

The fly stock (*chaGal4;UAS-Rab4-mRFP*) were reared at 25°C on standard corn agar meal with 12-hour light-dark cycle. Unless otherwise mentioned, the eggs were collected for an hour and kept at 25°C for aging until 78 hours. Third instar larvae were dissected in Jan and Jan Buffer (pH=7.2) containing 128 mM NaCl, 2 mM KCl, 4 mM MgCl<sub>2</sub>, 1.8 mM CaCl<sub>2</sub>, 35.3 mM Sucrose and 5 mM HEPES, through a dorsal incision along the posterior-anterior axis. After removal of the internal organs, the preps were placed on coverslips for immediate live imaging. The fillet prep was mounted with cuticle side facing towards the coverslip or reversed for imaging of the lateral chordotonal (*lch5*) neurons and ventral ganglion, respectively.



**FIG. 3: Thought Experiment:** (A) Schematics of the thought experiment - A bunch of balls color coded according to their velocities are lined up at the starting point of a multi-lane track of length  $L$ . The balls are arranged according to their velocities - with the slowest one at one end (red ball) and the fastest one at the other (green ball). They move smoothly on their respective track on which the starting point and the finishing point are denoted by a red dotted line. All the balls start moving simultaneously towards the finish point on their respective tracks, but ultimately their velocities determine the time they take to complete their move. The first five snapshots of the system clicked at regular intervals by a virtual camera of fixed pixel size. (B) Three kymographs for the tracking experiment on three separate multilane tracks of different length are shown (Set-1:  $1.0 \mu\text{m}$ , Set-2:  $1.5 \mu\text{m}$  and Set-3:  $2.0 \mu\text{m}$ ). The motion of the ball of a given color is captured by a segmental run of the same color on the kymograph. From each kymograph, we get an ensemble of runs having same runlength but different velocities (isoruns). (C) Velocity vs Runlength plot made by stacking the isoruns obtained from different kymographs (dots). The solid grey lines are the corresponding curves obtained from equation (4) ( $\Delta\ell=0.1 \mu\text{m}$  and  $\Delta t = 0.2 \text{ s}$ ) for different values of  $m$  and  $n$ . The blue horizontal lines represent isoruns and the vertical lines represent the isovels.  $m^{\text{th}}$  cluster is demarkated by the rectangles the top of the plot.



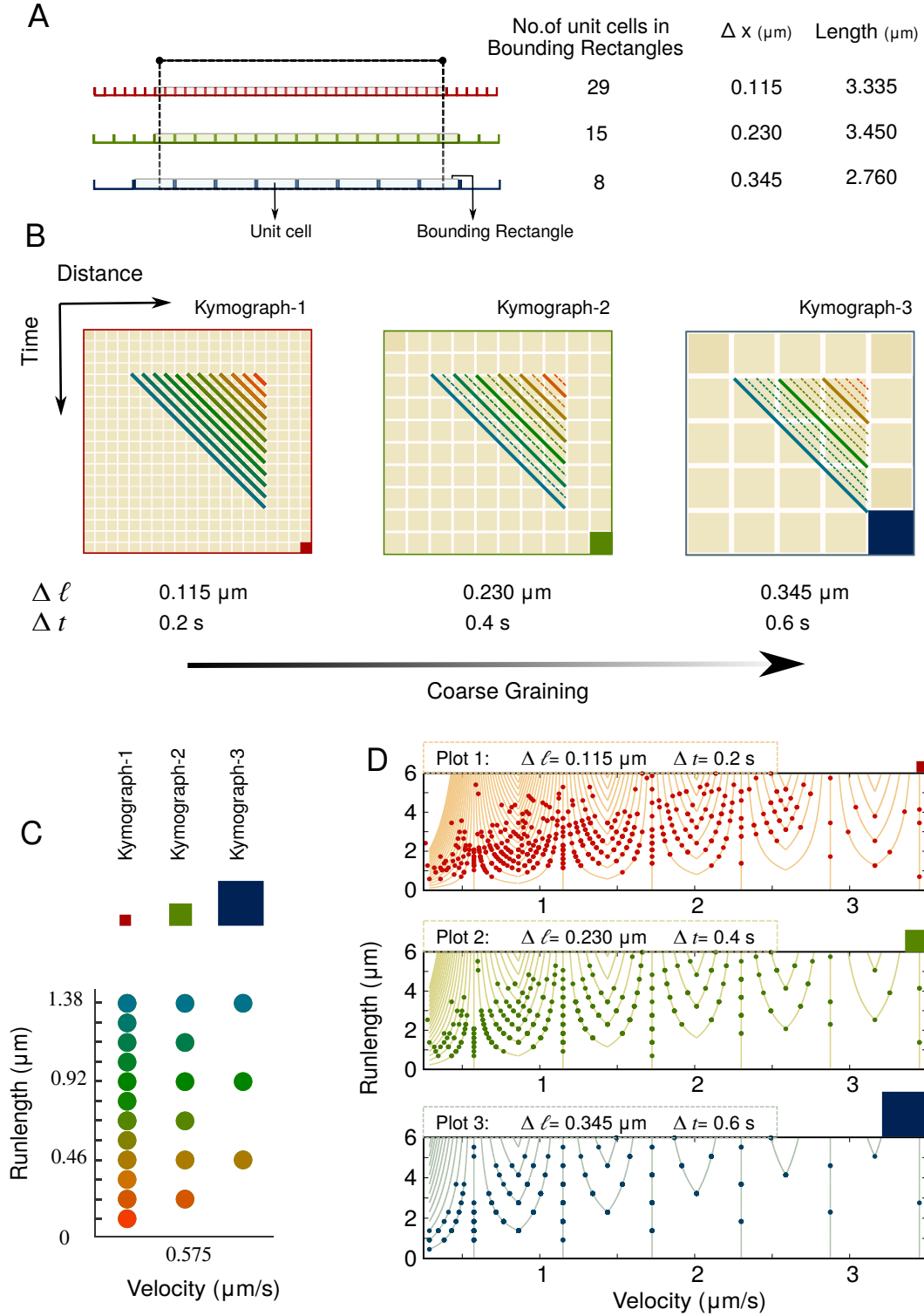


**FIG. 4: Effect of Space and Time resolution on runlength-velocity plots:** (A) A linear segment when measured by three rulers of different spatial resolution  $\Delta x$ , yields different results as summarised in the table complementing the figure. (B) An ensemble of runs having same velocity but different runlengths are recorded on three different kymographs having different pixel dimensions (spatial and temporal resolution). The leftmost kymograph with red boundaries has the maximum resolution whereas the rightmost kymograph with blue boundaries has the minimum resolution. Resolution of each kymograph is indicated below it and can be qualitatively compared with the colored cells at the corner of each kymograph. In all the kymographs, the solid lines can be resolved perfectly but the dotted ones cannot be resolved perfectly due to inadequate resolution. But for the runs represented by dotted lines, the cells in which the run begins and the one in which the run ends will determine the magnitude of run length and run time. (C) Velocity and run lengths of the runs in three different kymographs are plotted with color-coded points. (D) Coarse grained anterograde runs obtained from experiments are plotted and fitted by equation (4) with values of  $\Delta \ell$  and  $\Delta t$  listed in (B) under the corresponding kymographs.

### Imaging vesicle motility in vivo

The vesicular movement was recorded (using a 60x 1.4 NA objective) from the proximal axonal segments of lch5 neurons visible as a flat stretch within a rectangular ROI (40.6 X 11.5  $\mu\text{m}^2$ ) region for 2 minutes. The movement of Rab4-mRFP vesicles was observed as bidirectional with a succession of anterograde and retrograde motions.

### Calculation of vesicular motility parameters

The vectorial motion of vesicles was analyzed from their respective kymographs constructed by Multiple kymograph plugin of ImageJ on *Drosophila* axons. Lines were drawn on the diagonal traces representing a run of minimum 1.0 psf separation (0.3  $\mu\text{m}$ ) and the information of angle, and length was translated into velocity and run length.

### Curve Fitting

The experimental data is analyzed and depicted with the help of Origin (<http://www.originlab.com/>) software. The peaks in the frequency distribution plots are assessed by the peak finder module of Origin (<http://www.originlab.com/>) using the first derivative method. The curve fits were converged with 2 tolerance value of  $10^{-6}$  and coefficient of determination between 0.92 to 0.95.

### Minimal Model and the algorithm for its Simulation

The minimal model should retain the features of both the axonal transport of vesicles and the imaging microscope. A one dimensional lattice with lattice unit 8 nm, resembles the microtubule whereas the self-driven particle hopping stochastically on the linear lattice mimics the cargo-motor complex moving in the noisy environment. The lattice along with the particle is imaged by an virtual camera of certain spatial ( $\Delta\ell=40$  nm) and temporal ( $\Delta t = 1.0$  s) resolution. The particle used is large enough (40 nm) to be resolved by the camera but the timescale ( $\Delta t_p$ ) and lengthscale ( $\Delta\ell_p$ ) of its hopping is smaller than the resolution. The particle (its left tip) situated initially at lattice site  $i$  (where  $i$  is a positive integer and  $i = 1, 2, \dots, L$ ), can either hop to the neighboring site on its right with probability  $p_r$ , or hop to the neighboring site on its left with probability  $p_l$  or remain at its current position with probability  $p_s$ . All these three probabilities are normalized in the sense that  $p_r + p_l + p_s = 1$ . And as the distance between the neighboring site is 8 nm, the lengthscale of the particle's movement is  $\Delta\ell_p = 8$  nm. We simulated the stochastic bidirectional movement of the particle using Monte-Carlo (MC) simulation. In each MC step, which takes place after  $\Delta t_p = 0.2$  s, a random number  $r$  ( $0 < r < 1$ ) is generated. If

- (i)  $r < p_r$  : the particle at site  $i$  moves to the site  $i + 1$  (distance  $\Delta\ell_p = 8$  nm) and its position is updated.
- (ii)  $p_r < r < p_r + p_l$  : the particle at site  $i$  moves to the site  $i - 1$  (distance  $\Delta\ell_p = 8$  nm) and its position is updated.
- (iii)  $p_r + p_l < r < p_r + p_l + p_s$  : the particle at site  $i$  remains there undisturbed.

As  $\Delta t = 5\Delta t_p$ , so after every 5 MC steps, a snapshot of the system is taken by the camera with spatial resolution  $\Delta\ell = 40$  nm. The whole algorithm can be understood from the figure SI Fig. 5.

The location of the particle in a particular frame will be denoted by the X-axis coordinate of the pixel on which the image of the particle is captured (SI Fig. 6 A-B ). We have shown the original trajectory of the simulated particle on a space time diagram (SI Fig. 6C), the kymograph generated by the virtual camera (SI Fig. 6D), and the segmental runs drawn on the kymograph for further analysis (SI Fig. 6E).

Furthermore, in SI Fig.7, we have shown nine different cases (patterns) with combinations of spatial and temporal resolution.

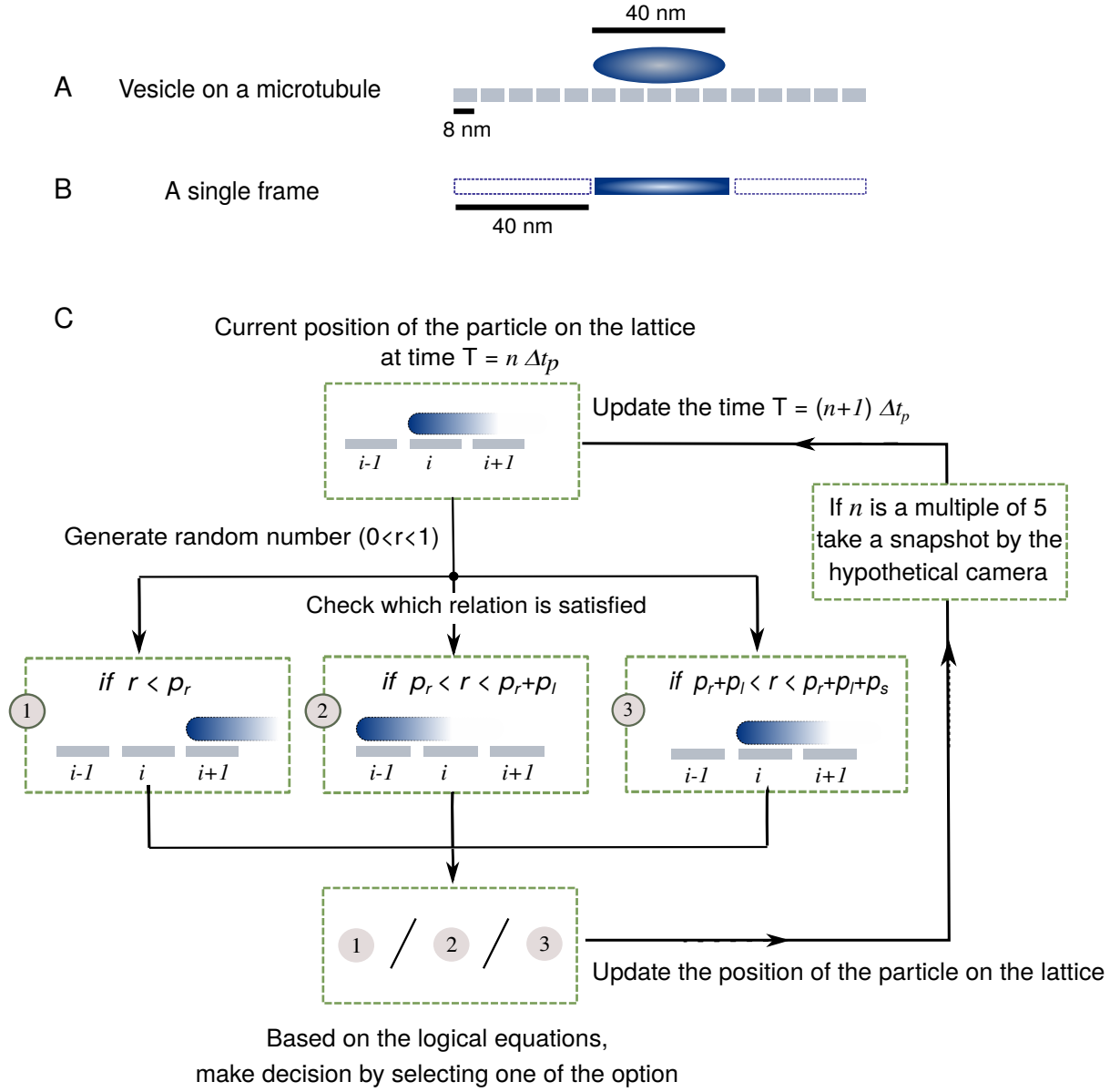


FIG. 5: **Minimal model and algorithm for simulating it:** (A) Self driven particle of length 40 nm on a lattice of lattice unit 8 nm. (B) A snapshot (frame with pixel size  $\Delta \ell = 40$  nm) capturing the particle. (C) Steps of the algorithm used for simulating the system using MC methods.

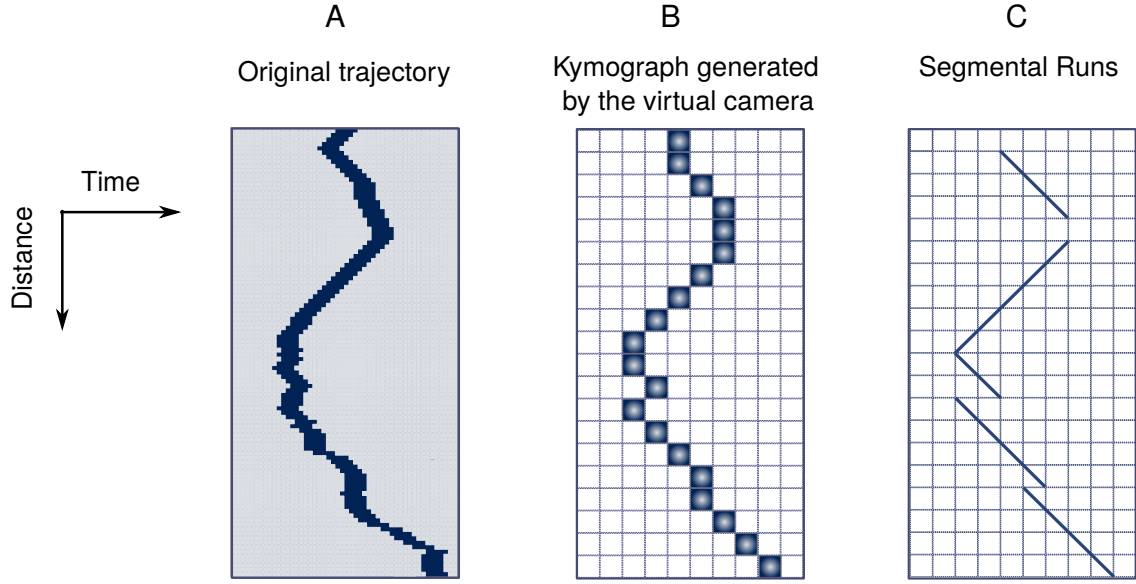


FIG. 6: (A) Original trajectory of the particle on the space-time diagram. (B) Kymograph generated by the virtual camera of  $\Delta\ell = 40$  nm and  $\Delta t = 1.0$  s. (C) Kymograph with segmental runs.

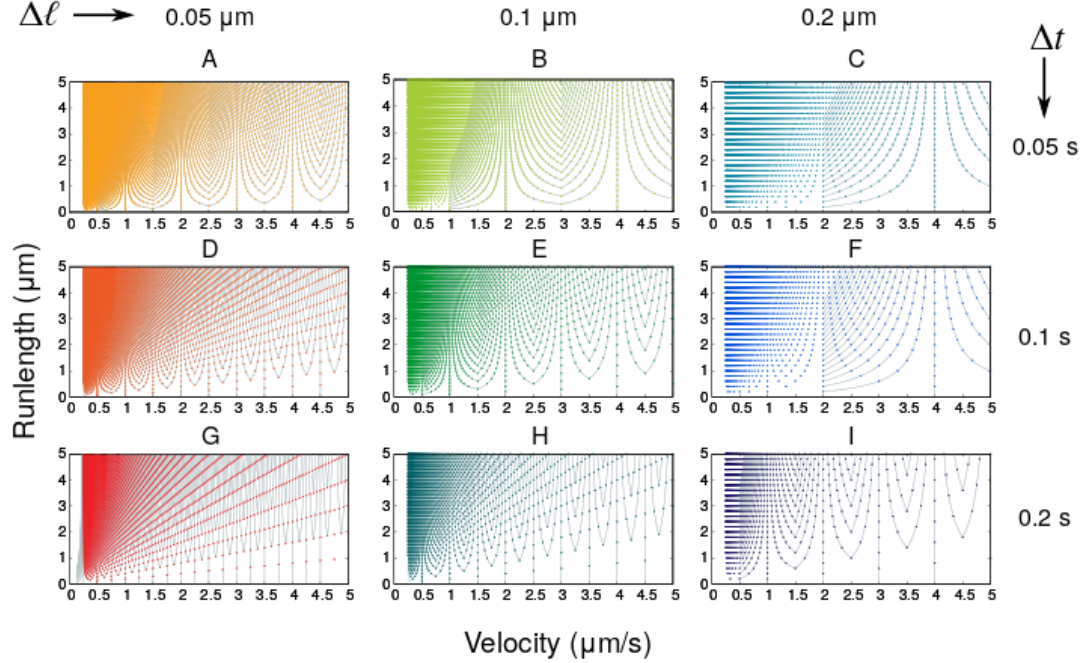


FIG. 7: **Patterns generated with different  $\Delta\ell$  and  $\Delta t$ :** (A)  $\Delta\ell = 0.05$   $\mu\text{m}$ ,  $\Delta t = 0.05$  s (B)  $\Delta\ell = 0.1$   $\mu\text{m}$ ,  $\Delta t = 0.05$  s (C)  $\Delta\ell = 0.2$   $\mu\text{m}$ ,  $\Delta t = 0.05$  s (D)  $\Delta\ell = 0.05$   $\mu\text{m}$ ,  $\Delta t = 0.1$  s (E)  $\Delta\ell = 0.1$   $\mu\text{m}$ ,  $\Delta t = 0.1$  s (F)  $\Delta\ell = 0.2$   $\mu\text{m}$ ,  $\Delta t = 1.0$  s (G)  $\Delta\ell = 0.05$   $\mu\text{m}$ ,  $\Delta t = 0.2$  s (H)  $\Delta\ell = 0.1$   $\mu\text{m}$ ,  $\Delta t = 0.2$  s (I)  $\Delta\ell = 0.2$   $\mu\text{m}$ ,  $\Delta t = 0.2$  s